Title:

Influence of nanovoids in the hydrogen embrittlement fracture of Al-Zn-Mg-Cu alloys

Authors:

Kazuyuki Shimizu[*a], Hiroyuki Toda[a], Chihiro Kadogawa[a], Hiro Fujihara[a], Akihisa Takeuchi[b],

Affiliations:

a Department of Mechanical Engineering, Kyushu University, Fukuoka, 819-0395, Japan

b Japan Synchrotron Radiation Research Institute, Hyogo, 679-5198, Japan

***Corresponding author:**

Name: Kazuyuki Shimizu

Affiliation: Department of Mechanical Engineering, Kyushu University, Motooka 744, Nishi-ku, Fukuoka-city, Fukuoka, 819-0395, Japan

Phone: +81-92-802-3300

E-mail: kshimizu@kyudai.jp

Abstract

Al-Zn-Mg alloys are representative high-strength aluminum alloys, but hydrogen embrittlement hinders further strengthening. The role of nanovoids in the hydrogen embrittlement of a hydrogen-charged Al-Zn-Mg-Cu alloy is examined using high-resolution imaging-type synchrotron X-ray tomography. Although nanovoids are initiated during deformation, their growth and coalescence behaviors are limited. Hydrogen partitioning analysis indicates that this is because most of the formed vacancies are not stabilized because of the low hydrogen occupancy. Furthermore, 3D/4D clustering analyses of nanovoids reveal that they do not aggregate on a specific plane to initiate a crack, and that linkage between nanovoids is less likely to occur.

Keywords: Hydrogen embrittlement, aluminum alloys, nanovoids, synchrotron X-ray tomography, 3D image analysis

1. Introduction

Hydrogen in the aluminum alloys is partitioned not only to the lattice but also to various trap sites such as vacancies [1,2], dislocations [3], precipitates [4], grain boundaries [5], and pores [6]. This trapped hydrogen leads to degrade the mechanical properties, especially in Al-Zn-Mg(-Cu) alloys [7–9]. Considering that susceptibility to hydrogen embrittlement increases with an increase in strength [7,10], the understanding and suppression of hydrogen embrittlement are essential for developing next-generation Al-Zn-Mg(-Cu) alloys.

The initiation and growth behaviors of hydrogen-induced nanovoids have been investigated in hydrogen-charged wrought Al-Zn-Mg-Cu alloys [11,12]. Su *et al.* revealed that nanovoids were formed in a wide size range from several nanometers to 1 μm in the flow localized region in the hydrogen-charged Al-Zn-Mg-Cu alloy after 5% strain [2]. Previous studies have suggested that hydrogen-induced nanovoids can potentially function as the origin of hydrogen-induced cracking and as hydrogen trap sites in materials [13–16].

Numerical studies employing first-principles and molecular dynamics simulations have revealed that the embryo of hydrogen-induced nanovoids is hydrogen-trapped vacancies [17–19]. The vacancies are stabilized by hydrogen, forming vacancy clusters and hydrogen–vacancy complexes. These clusters and complexes further aggregate into nanovoids. These numerical studies explored the nature of nanovoid formation based on hydrogen-trapped vacancies; however, in real materials, hydrogen is partitioned not only into vacancies but also into other trap sites such as dislocations, grain boundaries, eutectic particles, and precipitates, depending on the binding energy and trap-site density [2,4,13,20–23]. Therefore, by analyzing the hydrogen partitioning throughout

the entire material, the quantification of hydrogen occupancy in the vacancies can be used to reasonably interpret nanovoid formation and growth.

In experimental studies, it has been argued that the growth and coalescence of nanovoids induce a quasi-cleavage crack in steels. Martin *et al.* reported that nanovoids initiated at slip-band intersections generate quasi-cleavage cracks, resulting in the characteristic pattern of quasi-cleavage facets [24,25]. Neeraj *et al.* documented the contribution of the growth and coalescence of nanovoids to the propagation of quasi-cleavage cracks in the strain-localization region based on the observation of the quasi-cleavage surface [26,27]. These reports present indirect evidence of the involvement of nanovoids in hydrogen embrittlement fracture based on the presence of contrast corresponding to them on the characteristic fracture surface. Furthermore, the nature of nanovoids in steels with body-centered cubic structures may completely differ from that in aluminum alloys with face-centered cubic structures.

The visualization of nanovoid growth and coalescence behavior, and the related crack initiation, provides direct evidence of the role of nanovoids in hydrogen embrittlement. Although the quantitative analysis of deformation and damage behaviors within bulk materials can be realized with in situ observation using projection-type synchrotron X-ray tomography, it is impossible to visualize nanovoids using this method because the spatial resolution is limited to approximately 1 μm [28]. More recently, Fresnel zone plates with apodized apertures have been developed in SPring-8, Japan, enabling 100 nm-resolution imaging-type synchrotron X-ray tomography in bulk materials [29]. In this study, the 3D/4D direct visualization of nanovoids in Al-Zn-Mg-Cu alloy was realized utilizing imaging-type X-ray tomography, and the role of nanovoids in the alloy's fracture behavior was investigated. Nanovoid initiation and growth

behaviors were evaluated based on the hydrogen trapped in the vacancies by analyzing hydrogen partitioning in the Al-Zn-Mg-Cu alloy. Furthermore, the 3D clustering of nanovoids was quantitatively analyzed to evaluate nanovoid coalescence and aggregation tendencies in a specific plane.

2. Methodology

An overaged Al-Zn-Mg-Cu alloy with a chemical composition of Al along with (in mass%) 9.9 Zn, 2.3 Mg, 1.4 Cu, 0.06 Si, 0.05 Fe, 0.04 Ti, and 0.15 Zr was used in this study. The ingot was homogenized at 743 K for 24 h, hot-rolled at 673 K, solution-treated at 748 K for 2 h, and artificially aged at 393 K for 6 h and 423 K for 5 h. After aging, the prepared alloy was machined along the rolling direction by a wire-cut electrical discharge machine (EDM) using distilled water for in situ tensile tests. Fig. 1 shows the geometry of an in-situ tensile test specimen; its gauge length and cross-sectional area are 0.7 mm and 0.6 mm × 0.6 mm, respectively. EDM was also used for increasing the hydrogen content in specimens. Using a vacuum fusion method, we have already demonstrated that the hydrogen content can be increased from 0.14 to 6.97 mass ppm with EDM in purified water [30]. To distribute the hydrogen to the interior of the specimens, the specimens were stored in acetone for approximately 4 days and subjected to tomographic experiments, as described later. Assuming that the diffusion coefficient of the hydrogen in aluminum at 300 K was 2.19×10^{13} m^2/s [31,32], the diffusion distance after 4 days was estimated to be 0.38 mm. This diffusion distance is larger than half of the specimen size, and the hydrogen is thus assumed to have diffused from the surfaces to the centers of the specimens. The precipitate of this alloy has been observed to be η phase ($MgZn_2$) by means of high-angle annular dark-field scanning transmission electron microscopy

HAADF-STEM [12]. The η_2 phase with a coherent interface was also observed in alloys with compositions and heat treatment histories similar to those used in this study [33,34], and it was assumed that the precipitate interface of the overaged alloy used in this study was coherent. As described later, the coherent interface of a precipitate behaves as a strong trap site for hydrogen.

In situ observation of the nanovoid evolution behavior through imaging-type X-ray tomography was performed at BL20XU of SPring-8, Japan. Fig. 1 of [29] depicts the experimental configuration. A tensile testing machine (DEBEN 500 CT) was installed on the rotation stage. The X-ray used was monochromated by an Si (111) double-crystal monochromator and tuned to 20 keV. Scanning over 180° in 0.1° increments, 1800 projection images were obtained through tomographic observation. The exposure time of each projection was 500 ms and the total acquisition time of one tomographic scan was approximately 1 ks. After observations, a series of projections was reconstructed into a 3D image using the convolution back-projection algorithm [35]. The isotropic voxel size of the reconstructed image was 64 nm. For the in situ tensile tests at room temperature, tomographic scanning was performed at 0% applied strain and at the subsequent plastic strain levels. Here, the strain increment was set to approximately 2%. The initial strain rate was set to 3×10^{-3} s^{-1} by displacement control.

In the obtained 3D tomographic images, various geometrical features of the nanovoids and pores, such as the center of gravity, volume, surface area, and diameter, were individually computed using the marching cubes algorithm [36]. To eliminate inaccuracies originating from image noise, features more than nine voxels in volume alone were classified as nanovoids, particles, and pores. Identical nanovoids and pores at different loading steps were tracked in reverse chronological order from the last loading

step to the no-loading state using the microstructural feature tracking technique [37,38]. When a given nanovoid could not be further tracked under a specific applied strain level, it was assumed to have been initiated at that applied strain level.

3. Initiation and evolution behavior of nanovoids

Figs. 2 (a–d) depict the initiation and evolution behaviors of nanovoids in the Al-Zn-Mg-Cu alloy during deformation. Figs. 2 (a) and (b) show the 2D tomographic virtual cross-sections at applied strains ε_a of 1.6% and 3.3% respectively, indicating that nanovoids are initiated at ε_a = 3.3%. Here, we define initiation as the point at which the nanovoid size exceeds 100 nm, which is the physical limit of the imaging in this study, in diameter. In addition, nanovoids of several and several tens of nanometers in diameter have been observed at the applied strain of 5% using HAADF-STEM [12], suggesting that nanovoids smaller than 100 nm exist at an applied strain of less than 3.3%. Nanovoids are not initiated heterogeneously on particles such as Al_7Cu_2Fe and Mg_2Si, indicating that their origin is neither the cracking nor the interfacial decohesion of particles. In situ tomographic observations are repeated until fracture (Fig. 2 (c)), and the initiation and evolution behaviors of the nanovoids and preexisting pores are analyzed using the microstructural features tracking technique (Fig. 2 (d)) [37]. Here, as described in the methodology, identical nanovoids are specified in the 3D tomography images through tensile loading, and then identical nanovoids are tracked in reverse chronological order from the last loading step to the no-loading state. The initiation strain of an individual nanovoid is defined as the strain at which the nanovoid cannot be further tracked. In Fig. 2 (d), the nanovoids and pores have been evaluated separately. In this study, a pore is defined as a hydrogen-filled pre-existing void in the aluminum alloy, and a nanovoid is

defined as a void of less than 1 μm in diameter initiated after tensile loading. The coalescence of pores and microvoids has been revealed to be dominant in the ductile fracture of Al-Cu-Mg alloys and duplex stainless steels, respectively [38,39]. Neither of these phenomena is shown in Fig. 2 (d). This is because the fracture mode of the alloy used in this study is hydrogen embrittlement fracture, not ductile fracture. It is observed that the nanovoid volume fraction is several times lower than that of the pores immediately before fracture. The nanovoid volume fraction and mean equivalent diameter are 4.3×10^{-5} and 2.5×10^{-7} m at 8.9% ε_a, respectively. The nanovoids initiated at 1.6% ε_a do not grow significantly throughout loading, and their volume fraction is 1.9×10^{-7} at 8.9% ε_a. Limited nanovoid evolution during deformation is unexpectedly totally different from that of microvoids in ductile fracture.

In tomographic experiments, the displacement was held at each strain level as the observation was performed. Stress relaxation during displacement holding appears as a stress drop, as shown in Fig. 2. (c), resulting in a decrease in the hydrostatic stress and internal residual stresses. This periodic decrease in local elastic stress may affect the stability of voids and vacancy clusters, leading to limited nanovoid evolution during deformation. However, the influence of hydrostatic stress on the growth of nanovoids in the Al-Zn-Mg-Cu alloy used is minor. No nanovoids exceeding 100 nm were observed near quasi-cleavage cracks with high hydrostatic stress fields in a previous report [40]. This trend was derived from a similar high-resolution tomographic observation using the same specimen in this study. Therefore, we argue that the effect of hydrostatic stress on the growth of nanovoids of at least 100 nm is minor.

4. Hydrogen partitioning to vacancies

As previously mentioned, the embryo of a nanovoid is a vacancy stabilized by hydrogen. The limited evolution (Fig. 2 (d)) is due to either nonabundant vacancies for nanovoid growth or insufficient hydrogen for stabilizing the existing vacancies. Hydrogen in aluminum alloys is partitioned not only to the vacancies but also to other trap sites depending on the occupancy, θ, and trap site density, N, modeled as follows [13,20,40]:

$$C_{\mathrm{H}}^{\mathrm{total}} = \theta_{\mathrm{L}} N_{\mathrm{L}} + \sum \theta_i N_i + C_{\mathrm{pore}}, \tag{1}$$

where $C_{\mathrm{H}}^{\mathrm{total}}$ is the total hydrogen content in the alloy, and subscripts L and i are the normal interstitial lattice site and i-th trap site, respectively. C_{pore} is the total molecular hydrogen content in the pores [13,20,41]. According to [42], θ_i is calculated by assuming local thermal equilibrium between the interstitial and i-th trap sites:

$$\frac{\theta_i}{1-\theta_i} = \theta_{\mathrm{L}} \exp\left(\frac{E_i}{RT}\right), \tag{2}$$

where R is the gas constant and T is the temperature. The hydrogen trap sites include vacancies, solute atoms, edge/screw dislocations, grain boundaries, precipitate interfaces, intermetallic particles, and pores; their reported binding energies are 29.0 [2,21], 11.6 [43], 16.4/7.7 [3], 19.3 (at $\Sigma 5\{012\}$ grain boundary) [5], 7.9–33.9 [4], 28.1 [44], and 67.5 [6] kJ/mol, respectively. The trap site density at each site in Eq. (1) has been quantified by experiments or mathematical models [13,20]. For instance, the dislocation density corresponding to the dislocation trap-site density was quantified based on the plastic strain within the alloy, computed using the microstructural tracking technique [13], and the precipitate density was quantified using a transmission electron microscope [33,34,45]. Details regarding the hydrogen partitioning calculation and quantification of the trap-site densities other than the vacancies are available elsewhere [13,20].

The previously proposed hydrogen partition calculations assume that all the vacancies formed during deformation are stabilized by hydrogen [13,20]. The vacancy concentration is estimated by ignoring annihilation and considering only formation [13,20]. As all the vacancies are not stabilized by hydrogen, we precisely calculated the vacancy concentration considering both formation and annihilation. Militzer *et al.* presented the excess vacancy concentration, $C_{\mathrm{v}}^{\mathrm{ex}}$, based on the nonconservative jog motion during deformation [46]:

$$C_{\mathrm{v}}^{\mathrm{ex}} = C_{\mathrm{v}}^{0} + C_{\mathrm{v}}^{\mathrm{s}}\left\{1 - \exp\left[-D_{\mathrm{V}}\left(\frac{\rho_{\mathrm{S}}}{\kappa^2} + \frac{1}{L^2}\right)t_{\mathrm{load}}\right]\right\}, \tag{3}$$

where C_{v}^{0} is the initial vacancy concentration, D_{v} is the diffusion coefficient of the vacancy (1.2×10^{-16} m^2/s at 300 K [47]), ρ_{s} is the dislocation density, k is the structural dislocation parameter (assumed to be unity), L is the grain size, and t_{load} is the load application time. $C_{\mathrm{v}}^{\mathrm{s}}$ is the steady-state vacancy concentration, defined by Militzer *et al.* [46]. As shown in Fig. 2 (c), it is necessary to suspend monotonic loading and hold the displacement during scanning in in situ tomographic experiments. This holding time, t_{hold}, was set to 3.3 ks in this study. Excess vacancies were presumed to annihilate while holding the displacement. Regarding vacancy annihilation, Militzer *et al.* modeled the following equation based on the absorption of vacancies by dislocations [46]:

$$C_{\mathrm{v}}^{\mathrm{anni}} = C_{\mathrm{v}}^{0} + C_{\mathrm{v}}^{\mathrm{ex}}\exp\left[-D_{\mathrm{V}}\left(\frac{\rho_{\mathrm{S}}}{\kappa^2} + \frac{1}{L^2}\right)t_{\mathrm{hold}}\right], \tag{4}$$

where $C_{\mathrm{v}}^{\mathrm{anni}}$ is the vacancy concentration after t_{hold}. Using Eqs. (3) and (4), the vacancy concentration during in situ tomographic experiments was estimated and assigned to one of the hydrogen trap site densities in Eq. (1).

Hydrogen partitioning at 0% and 8.9% ε_{a} was analyzed by combining Eqs. (1) and (2), and the trapped hydrogen content and hydrogen occupancy at each site were

obtained (Table 1). The hydrogen vacancy occupancies were notably low at 4.3×10^{-3} and 3.0×10^{-3} at 0% and 8.9% ε_a, respectively. The trapped hydrogen content in the vacancies was increased because numerous vacancies were formed by deformation, but the hydrogen vacancy occupancy remained low. This occupancy is unity when one vacancy traps eight hydrogen atoms [21]; therefore, the average number of trapped hydrogen atoms in a vacancy is 3.4×10^{-2} and 2.4×10^{-2} at 0% and 8.9% ε_a, respectively. Nanovoid evolution and the change in the vacancy concentration are depicted in Fig. 3 (a), indicating that the vacancy concentration formed by monotonic loading is one order of magnitude greater than the nanovoid volume fraction. As shown in Fig. 3(b), on increasing the applied strain levels, the hydrogen occupancy of the vacancies is decreased rather than increased, indicating that many of the vacancies formed are not stabilized by hydrogen and do not grow into nanovoids because of the low hydrogen vacancy occupation. Hence, the limited nanovoid evolution in Fig. 2 (d) can be attributed to the absence of hydrogen for stabilizing the abundantly formed vacancies.

The vacancy concentration during holding drops to the order of 10^{-8} (Fig. 3 (a)). Vacancy annihilation is based on vacancy absorption by dislocations [46], which is strongly dependent on the dislocation structure. As it is difficult to assess the dislocation structure during holding, we assume a uniform dislocation distribution ($\kappa = 1$). The actual vacancy annihilation during holding may not drop to the order of 10^{-8}. However, vacancy formation (Eq. (3)) is calculated using an initial vacancy concentration, C_0, of the order of 10^{-8}, which is conservative in terms of vacancy formation.

5. Influence of nanovoids on the fracture

Fig. 4 indicates that the 3D nanovoid and pore distribution at each ε_a is

heterogeneous to a certain extent, with no rapidly growing singular nanovoids. No interaction between pores and nanovoids is observed. Concretely, no aggregation of nanovoids around the pores is observed in Fig. 4. If the growth of micrometer-order pores is promoted by nanovoids or hydrogen, dimple fracture, which comprises the growth and coalescence of pores, is enhanced in the alloy, but such results have not been observed in Al-Zn-Mg(-Cu) alloys. It is recognized that the pore is a kind of micrometer-level defect and that the triaxial stress around it is locally increased under external loading. As seen in Fig. 4, no characteristic nanovoid growth and aggregation are observed even in the high triaxial stress field near the pores. This result implies that the driving force for nanovoid aggregation and growth is not stress-controlled, which is consistent with the results in Fig. 3.

We investigated whether nanovoids agglomerate on a slip plane or specific crystallographic plane in the Al-Zn-Mg-Cu alloy, thus initiating a crack. The visualized nanovoid aggregation behavior was quantitatively analyzed. Nanovoid clustering was performed statistically, after which the linkage and geometric shape of the nanovoid distribution in each cluster were evaluated. For clustering, the k-nearest neighbor algorithm was used [48]. The 1^{st}–23^{rd} nearest neighbors were defined as one nanovoid cluster (k = 24); such clustering was performed for all observed nanovoids. At 8.9% ε_a, 205 nanovoids were present in the field-of-view, and the number of clusters was also 205. Here, the number of nanovoids in one cluster was set to 24 to satisfy a statistically significant sample size in the principal component analysis described later [49]. Although we also performed the analysis using nine nanovoids per cluster (k = 9), the conclusion of this study described later was not changed. After clustering, the maximum distance between the nearest nanovoid neighbors, d_{NN}, and the planarity of the nanovoid

distribution, P, were evaluated. P was defined as $P = \lambda_0 (\lambda_0 + \lambda_1 + \lambda_2)^{-1}$, where λ_0, λ_1, and $\lambda_2 (\lambda_0 \leq \lambda_1 \leq \lambda_2)$ are eigenvalues of the covariance matrix of the 3D nanovoid spatial coordinates in one cluster, generated by principal component analysis [50]. Figs. 5 (a–c) illustrate the nanovoid distribution in a cluster. If the nanovoid distribution is 3D isotropic or completely planar, P is 0.333 or 0, respectively. When the nanovoids are randomly distributed in a cluster, P is 0.231.

The computed d_{NN}, used for evaluating nanovoid linkage, and P in all the clusters at each applied strain level are plotted in Fig. 5 (d). Immediately before fracture (8.9% strain), the minimum d_{NN} is 3.2 μm. Finite element analysis has revealed that the stress intensity between nanovoids is significantly enhanced when the distance between them is less than five times the nanovoid diameter [51]. As the mean nanovoid diameter is 2.5×10^{-7} m, d_{NN} must be ≤1.25 μm to generate a linkage. In Fig. 5(d), d_{NN} is considerably greater than the minimum of 1.25 μm, and the nanovoid distribution is relatively discrete immediately before fracture. P was used to assess whether the nanovoids aggregate on planes. The average P of all the nanovoid clusters immediately before fracture (8.9%) was 0.131, indicating that the nanovoids in the clusters were between random and planar distributions and closer to the random distribution. Furthermore, it is unlikely that nanovoids aggregate rapidly after 8.9% ε_a because there are no significant changes in P between 5.9% and 8.9% ε_a. Hence, nanovoids are unlikely to agglomerate on a specific plane and coalesce to initiate cracks. Moreover, nanovoids have been detected even in Al-Mg-Si alloys whose mechanical properties are not degraded by hydrogen, and we cannot conclude that nanovoids influence hydrogen embrittlement fracture in aluminum alloys [52].

Imaging-type tomography in this study can visualize nanovoids over 100 nm

because of its spatial resolution. Such nanovoids are classified as relatively coarse; finer nanovoids have been observed in a 5% strained Al-Zn-Mg-Cu alloy employing HAADF-STEM [12]. As mentioned above, because d_{NN} and P did not significantly vary between 5.9% and 8.9% ε_a, it is difficult to speculate that fine nanovoids alone agglomerate on a specific plane, while maintaining a size below 100 nm.

In this study, because of the strict time limit of the synchrotron experiments, it was not possible to perform comparative analysis with no-hydrogen specimens. Therefore, it is impossible to strictly assess the influence of hydrogen on the nanovoid initiation and evolution. However, even if specimens without hydrogen were assessed, in specimens with high hydrogen contents, conclusions that nanovoid initiation and evolution are limited and the effect on hydrogen embrittlement fracture is less are not changed.

6. Conclusions

Hydrogen-induced nanovoids in Al-Zn-Mg-Cu alloys were visualized using imaging-type tomography, and their evolution behaviors and influences on fracture were quantitatively analyzed. Nanovoids of 100 nm or more in diameter were assessed and the nanovoid evolution behavior was found to be limited by the low hydrogen occupancy in the formed vacancies. Statistical analysis of the nanovoid aggregation behavior revealed that the nanovoid contribution to hydrogen embrittlement fracture is minor. It is suggested that nanovoids can trap enormous quantities of hydrogen, thus functioning as major hydrogen trap sites in Al-Zn-Mg-Cu alloys.

Acknowledgments

This research was supported by Japan Science and Technology Agency (JST) under Collaborative Research Based on Industrial Demand "Heterogeneous Structure Control: Towards Innovative Development of Metallic Structural Materials", Grant Number JPMJSK1412, Japan. This research was supported in part by a grant from the Light Metal Educational Foundation, Japan. The synchrotron radiation experiments were performed at the BL20XU of SPring-8 with the approval of Japan Synchrotron Radiation Research Institute (JASRI) (Proposal No. 2017B0076, 2018A0076, 2018B0076).

Reference

[1] L. Ismer, M.S. Park, A. Janotti, C.G. Van De Walle, Phys. Rev. B - Condens. Matter Mater. Phys. 81 (2010) 184110.
[2] T. Enomoto, R. Matsumoto, S. Taketomi, N. Miyazaki, Zair. Soc. Mater. Sci. Japan 59 (2010) 596–603.
[3] M. Itakura, M. Yamguchi, K. Ebihara, K. Matsuda, H. Toda, Prep. (n.d.).
[4] T. Tsuru, M. Yamaguchi, K. Ebihara, M. Itakura, Y. Shiihara, K. Matsuda, H. Toda, Comput. Mater. Sci. 148 (2018) 301–306.
[5] M. Yamaguchi, K.-I. Ebihara, M. Itakura, T. Tsuru, K. Matsuda, H. Toda, Comput. Mater. Sci. 156 (2019) 368–375.
[6] M. Yamaguchi, T. Tsuru, K. Ebihara, M. Itakura, J. Japan Inst. Light Met. 68 (2018) 588–595.
[7] R.G. Song, W. Dietzel, B.J. Zhang, W.J. Liu, M.K. Tseng, A. Atrens, (2004).
[8] G.M. Bond, I.M. Robertson, H.K. Birnbaum, Acta Metall. 35 (1987) 2289–2296.
[9] C.J. Mcmahon, Hydrogen-Induced Intergranular Fracture of Steels, n.d.
[10] M. Hirano, K. Kobayashi, H. Tonda, J. Soc. Mater. Sci. Japan 49 (2000) 86–91.
[11] H. Gao, H. Su, K. Shimizu, C. Kadokawa, H. Toda, Y. Terada, K. Uesugi, A. Takeuchi, Mater. Trans. 59 (2018) 1532–1535.
[12] H. Su, H. Toda, R. Masunaga, K. Shimizu, H. Gao, K. Sasaki, M.S. Bhuiyan, K. Uesugi, A. Takeuchi, Y. Watanabe, Acta Mater. 159 (2018) 332–343.
[13] H. Su, H. Toda, K. Shimizu, K. Uesugi, A. Takeuchi, Y. Watanabe, Acta Mater. 176 (2019) 96–108.

[14] T. Neeraj, R. Srinivasan, J. Li, Acta Mater. 60 (2012) 5160–5171.
[15] M. Nagumo, M. Nakamura, K. Takai, Metall. Mater. Trans. A 32 (2001) 339–347.
[16] S. Lynch, Corros. Rev. 37 (2019) 377–395.
[17] S. Li, Y. Li, Y.-C. Lo, T. Neeraj, R. Srinivasan, X. Ding, J. Sun, L. Qi, P. Gumbsch, J. Li, Int. J. Plast. 74 (2015) 175–191.
[18] J. Xiong, Y. Zhu, Z. Li, M. Huang, Scr. Mater. 143 (2018) 30–34.
[19] J. Hou, X.S. Kong, X. Wu, J. Song, C.S. Liu, Nat. Mater. 18 (2019) 833–839.
[20] K. Shimizu, H. Toda, H. Fujihara, K. Hirayama, K. Uesugi, A. Takeuchi, Eng. Fract. Mech. (2019) 106503.
[21] L. Ismer, M.S. Park, A. Janotti, C.G. Van De Walle, Phys. Rev. B - Condens. Matter Mater. Phys. 80 (2009).
[22] M. Yamaguchi, K. Ebihara, I. Mitsuhiro, T. Tsuru, Comput. Mater. Sci. (n.d.).
[23] R. Matsumoto, T. Enomoto, S. Taketomi, N. Miyazaki, in: Int. Hydrog. Conf. (IHC 2012), ASME Press, 2014, pp. 757–764.
[24] M.L. Martin, J. a. Fenske, G.S. Liu, P. Sofronis, I.M. Robertson, Acta Mater. 59 (2011) 1601–1606.
[25] I.M. Robertson, P. Sofronis, A. Nagao, M.L. Martin, S. Wang, D.W. Gross, K.E. Nygren, Metall. Mater. Trans. A Phys. Metall. Mater. Sci. 46 (2015) 2323–2341.
[26] T. Neeraj, R. Srinivasan, J. Li, Acta Mater. 60 (2012) 5160–5171.
[27] T. Neeraj, R. Srinivasan, in: Corrosion, 2017, pp. 437–447.
[28] H. Toda, K. Shimizu, K. Uesugi, Y. Suzuki, M. Kobayashi, Mater. Trans. 51 (2010) 2045–2048.
[29] A. Takeuchi, K. Uesugi, Y. Suzuki, J. Phys. Conf. Ser. 849 (2017) 012055.
[30] M.S. Bhuiyan, Y. Tada, H. Toda, S. Hang, K. Uesugi, A. Takeuchi, N. Sakaguchi, Y. Watanabe, Int. J. Fract. 200 (2016) 13–29.
[31] T. Ishikawa, R.B. McLellan, Acta Metall. 34 (1986) 1091–1095.
[32] Japan Institute of Light Metals, ed., Structures and Properties of Aluminum, Tokyo, 1991.
[33] A. Bendo, K. Matsuda, S. Lee, K. Nishimura, N. Nunomura, H. Toda, M. Yamaguchi, T. Tsuru, K. Hirayama, K. Shimizu, H. Gao, K. Ebihara, M. Itakura, T. Yoshida, S. Murakami, J. Mater. Sci. 53 (2018) 4598–4611.
[34] A. Bendo, K. Matsuda, S. Lee, K. Nishimura, H. Toda, K. Shimizu, T. Tsuru, M. Yamaguchi, (n.d.).
[35] A.C. Kak, M. Slaney, Principles of Computerized Tomographic Imaging, Society for Industrial and Applied Mathematics, 2001.

[36] W.E. Lorensen, H.E. Cline, W.E. Lorensen, H.E. Cline, in: Proc. 14th Annu. Conf. Comput. Graph. Interact. Tech. - SIGGRAPH '87, ACM Press, New York, New York, USA, 1987, pp. 163–169.
[37] M. Kobayashi, H. Toda, Y. Kawai, T. Ohgaki, K. Uesugi, D.S. Wilkinson, T. Kobayashi, Y. Aoki, M. Nakazawa, Acta Mater. 56 (2008) 2167–2181.
[38] H. Toda, A. Takijiri, M. Azuma, S. Yabu, K. Hayashi, D. Seo, M. Kobayashi, K. Hirayama, A. Takeuchi, K. Uesugi, Acta Mater. 126 (2017) 401–412.
[39] H. Toda, H. Oogo, K. Horikawa, K. Uesugi, A. Takeuchi, Y. Suzuki, M. Nakazawa, Y. Aoki, M. Kobayashi, Metall. Mater. Trans. A Phys. Metall. Mater. Sci. 45 (2014) 765–776.
[40] K. Shimizu, H. Toda, K. Uesugi, A. Takeuchi, Metall. Mater. Trans. A Phys. Metall. Mater. Sci. 51 (2020) 1–19.
[41] H. Toda, T. Hidaka, M. Kobayashi, K. Uesugi, A. Takeuchi, K. Horikawa, Acta Mater. 57 (2009) 2277–2290.
[42] R.A. Oriani, Acta Metall. 18 (1970) 147–157.
[43] T. Tsuru, S. Kazuyuki, Y. Masatake, I. Mitsuhiro, E. Kenichi, M. Kenji, H. Toda, Prep. (n.d.).
[44] H.G. Lee, J.Y. Lee, Acta Metall. 32 (1984) 131–136.
[45] A. Bendo, K. Matsuda, S. Lee, K. Nishimura, H. Toda, K. Shimizu, T. Tsuru, M. Yamaguchi, Materialia 3 (2018) 50–56.
[46] M. Militzer, W.P. Sun, J.J. Jonas, Acta Metall. Mater. 42 (1994) 133–141.
[47] K. Carling, G. Wahnström, T.R. Mattsson, A.E. Mattsson, N. Sandberg, G. Grimvall, Phys. Rev. Lett. 85 (2000) 3862–3865.
[48] B. Jutzi, H. Gross, R. Sensing, Int. Arch. Photogramm. Remote Sens. Spat. Inf. Sci. 38 (2009) 4–7.
[49] P.M. Kocovsky, J. V. Adams, C.R. Bronte, Trans. Am. Fish. Soc. 138 (2009) 487–496.
[50] M. Pauly, M. Gross, L.P. Kobbelt, Proc. IEEE Vis. Conf. (2002) 163–170.
[51] A. Weck, J. Segurado, J. Llorca, D. Wilkinson, H. Böhm, Int. J. Fract. 148 (2007) 205–219.
[52] M.A. Singh, S. Saimoto, M.R. Langille, J. Lévesque, K. Inal, A.R. Woll, Philos. Mag. 97 (2017) 2496–2513.

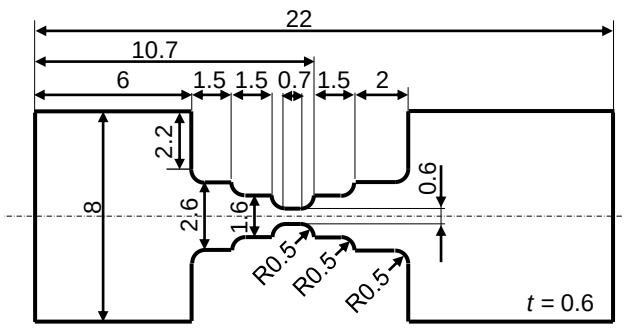

Fig. 1. Geometry of an in situ tensile test specimen machined by EDM. The gauge length and the cross-sectional area of the specimen are 0.7 mm and 0.6 mm × 0.6 mm, respectively.

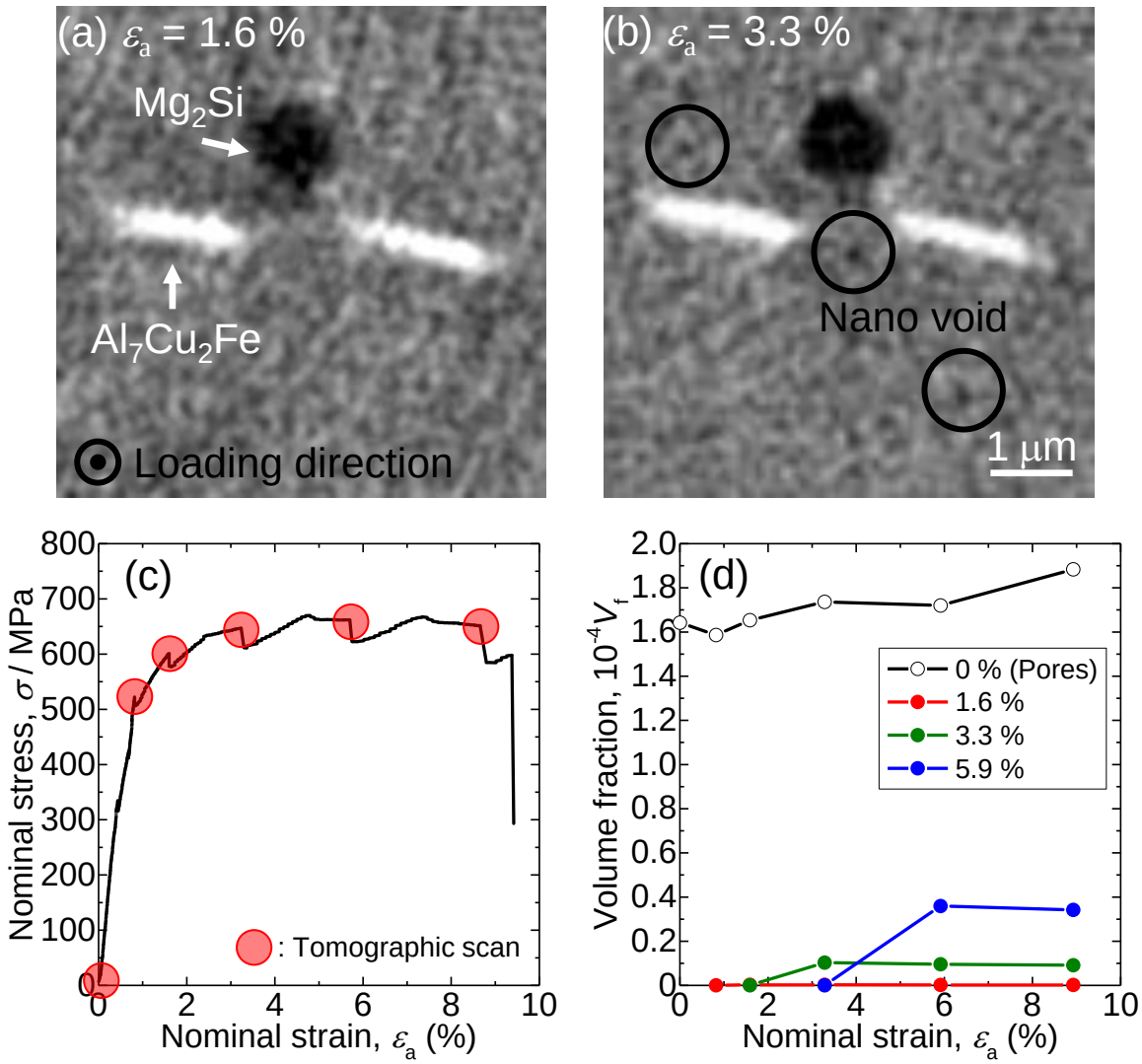

Fig. 2. Nanovoid initiation and evolution behavior in Al-Zn-Mg-Cu alloy during deformation: (a) and (b) 2D virtual cross-section under 1.6% and 3.3% strain, respectively; (c) Nominal stress–nominal strain curve of the used Al-Zn-Mg-Cu alloy (the strain levels at which tomographic scans are performed are indicated by red circles); (d) Changes in the nanovoid and pore volume fraction, V_f, during deformation (V_f of pores is indicated by a black line, whereas those of nanovoids initiated at applied strains of 1.6%, 3.3%, and 5.9% are indicated by red, green, and blue lines, respectively).

Table 1 Hydrogen partitioning calculations based on the hydrogen occupancies and hydrogen trap-site densities. It was assumed the total hydrogen content does not change during deformation.

	Trapped Hydrogen, C_H / atomH·m^{-3}		Hydrogen occupancy, θ	
Trap sites	ε_a = 0%	ε_a = 8.9%	ε_a = 0%	ε_a = 8.9%
Interstitial	7.1×10^{21}	4.9×10^{21}	3.9×10^{-8}	2.7×10^{-8}
Solute Mg atom	1.6×10^{21}	1.1×10^{21}	4.1×10^{-6}	2.8×10^{-6}
Vacancy	3.8×10^{18}	3.2×10^{24}	4.3×10^{-3}	3.0×10^{-3}
Dislocation	1.0×10^{18}	2.2×10^{17}	1.3×10^{-5}	9.3×10^{-7}
Grain boundary	2.0×10^{19}	1.4×10^{19}	8.9×10^{-5}	6.3×10^{-5}
IMC particle	5.0×10^{20}	3.5×10^{20}	3.0×10^{-3}	2.1×10^{-3}
Precipitate Interface	1.1×10^{25}	7.8×10^{24}	4.0×10^{-3}	2.8×10^{-3}
Pore and NV	2.9×10^{23}	3.9×10^{23}	9.9×10^{-1} [a]	9.9×10^{-1} [a]

[a] Occupancy of pores is shown due to that of NV cannot be defined.

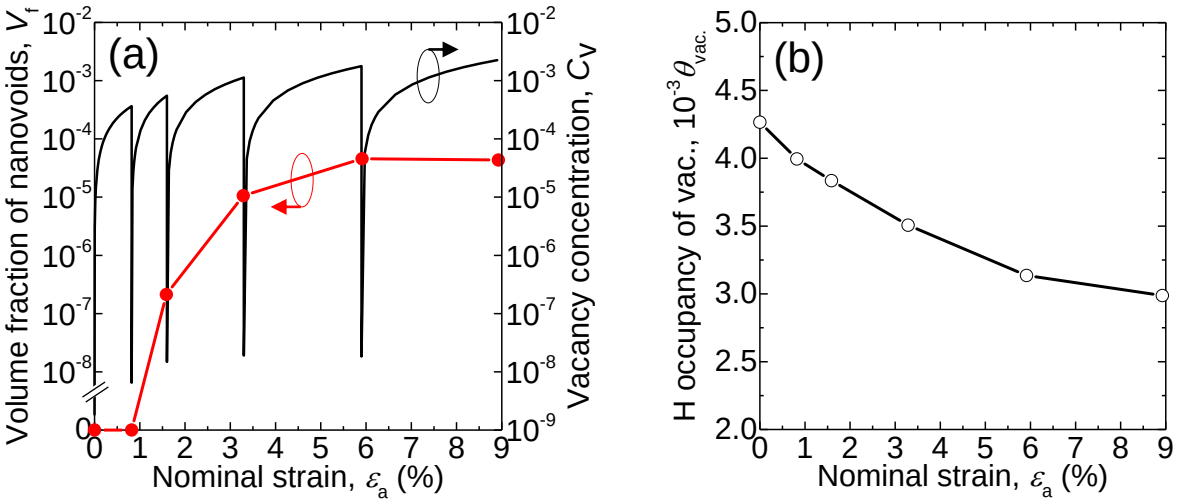

Fig. 3. (a) Comparison with the nanovoid volume fraction and vacancy concentration, and (b) hydrogen occupancy variation in the vacancies as a function of the applied strain.

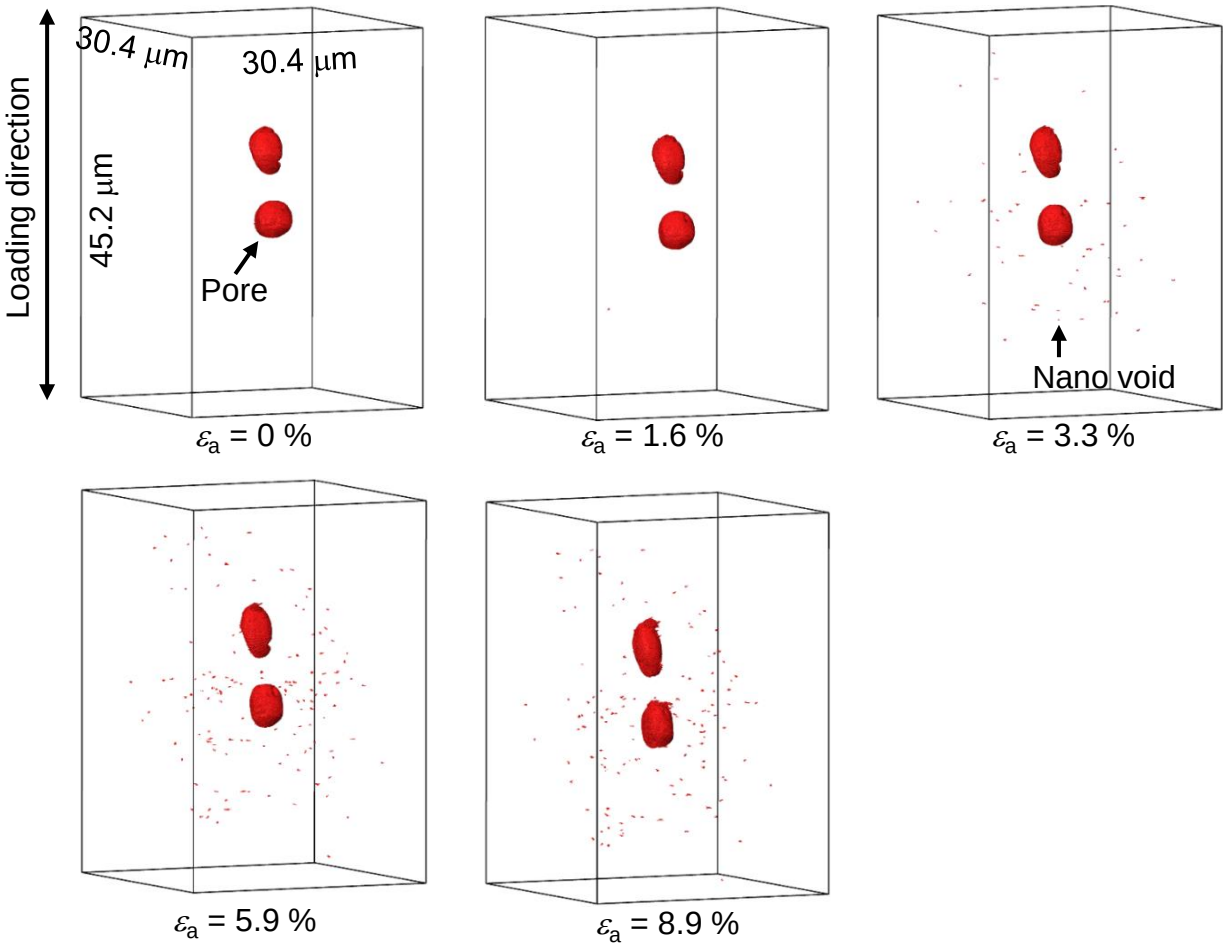

Fig. 4. 3D tomographic images of the pores and nanovoids in Al-Zn-Mg-Cu alloy at each applied strain level. The matrix and particles are depicted as transparent.

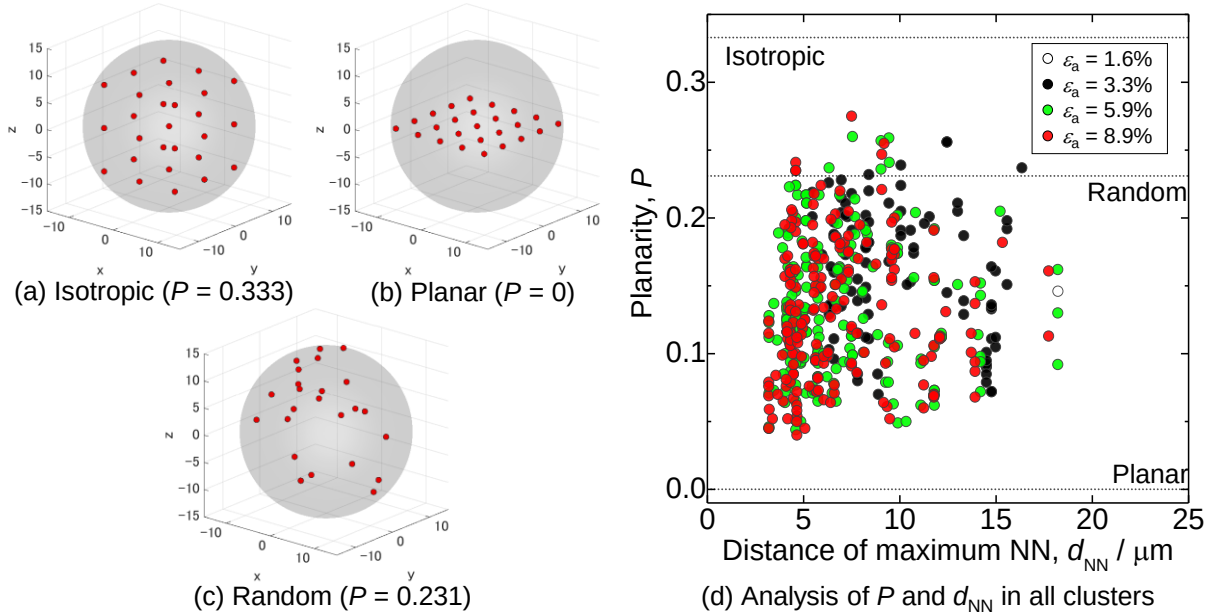

Fig. 5 Results of the nanovoid clustering analysis: (a–c) Nanovoids distribution in the cluster corresponding to each P; (d) Statistically analyzed P and d_{NN} in all the visualized nanovoid clusters.